Wear 516–517 (2023) 204605

Contents lists available at ScienceDirect

Wear

journal homepage: www.elsevier.com/locate/wear

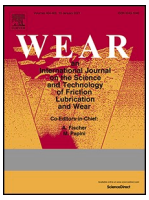

Preliminary investigation of slurry erosion behaviour of tantalum

J.S. Chouhan [a], B.D. Jana [a,b,*], Y.P. Purandare [a], A. Dey [c], P. Eh Hovsepian [a], D. Jenkins [c], L. Jones [c]

[a] Materials and Engineering Research Institute, Sheffield Hallam University, City Campus, Howard Street, Sheffield, S1 1WB, United Kingdom
[b] Department of Engineering and Mathematics, Sheffield Hallam University, City Campus, Howard Street, Sheffield, S1 1WB, United Kingdom
[c] Rutherford Appleton Laboratory, Didcot, OX11 0QX, UK

ARTICLE INFO

Keywords:
Slurry erosion
Erosion-mechanisms
Pure tantalum
Powder metallurgy

ABSTRACT

Frequent premature failure of the ISIS spallation neutron source target prompted the investigation of previously unexplored aqueous slurry erosion response of pure tantalum (Ta) with an overarching aim to improve the service life of the target; hence, reducing the disposal of radioactive waste. Understanding such response of Ta is highly significant to many other applications such as nuclear and chemical processing.

In this study, powder-metallurgically manufactured pure Ta was investigated with the help of an impinging jet aqueous slurry erosion apparatus using silicon carbide particles at a range of concentration, impact velocity, and incident angle. Results revealed a unique material removal mechanism consisting formation of extensive voids/cavities all over the eroded surface. These mechanisms are discussed considering the theories of solid particle erosion and the grain boundary sliding behaviour of Ta under localised indentation loading.

1. Introduction

1.1. Background and relevance

Tantalum (Ta) is a refractory metal with a high density of 16.67 gcm^{-3}, room temperature ductility (more than 20% tensile elongation) and extremely high corrosion resistance [1,2]. Approximately 900,000 kg of Ta is consumed annually worldwide in applications such as electronics, high-temperature ballistics, chemical processing, nuclear and biomedical [3]. Pure Ta is also used for manufacturing Ta cladded tungsten (W) neutron spallation source targets used by many neutron scattering facilities worldwide, including the ISIS facilities at Rutherford Appleton Laboratory (RAL) [4–8]. The Ta used in this application is manufactured via the powder metallurgy (PM) route, and it is bonded to the W target core by hot isostatic pressing [4,7]. The high melting point, high corrosion resistance and heavy nucleus make it one of the most popular choices for this application.

In many of the above applications, Ta may experience surface degradation and wear due to abrasive slurries. At RAL, the deionised water loop of the ISIS spallation target has been reported to experience a change in pH and contamination from radioactive isotopes of Ta/W (and many other transmuted isotopes) during its operation [9]. It is speculated that these contaminants, generated due to a combination of corrosion, erosion, and erosion-corrosion phenomena, lead to further degradation of the Ta cladding. This vicious cycle, eventually, is suspected to be responsible for the target premature failure under 2 years compared to its estimated lifetime of around 5 years. The operating condition makes the target radioactive; thereby leads to a further problem associated with target decommissioning and radioactive waste disposal. This demanded a thorough investigation of the erosion, corrosion and erosion-corrosion response of powder metallurgically manufactured Ta, which currently is less understood.

Solid particle erosion, under both aqueous slurry and dry conditions, has been extensively studied for most ductile and brittle materials [10–12]. However, aqueous slurry erosion response of Ta has not been explored sufficiently except for a publication available on water erosion [13]. Additionally, published erosion data is primarily available for metals synthesised via the melting and casting route, which may not relate to pure Ta manufactured via PM route. Components manufactured via PM route, depending on the powder size, compacting pressures, and sintering temperatures, may have non-uniform microstructures, differing grain sizes and porosity resulting in anisotropic mechanical properties [14,15]. As a result, it's response to slurry erosion (that involved microscopic events such as plastic deformation,

* Corresponding author. Materials and Engineering Research Institute, Sheffield Hallam University, City Campus, Howard Street, Sheffield, S1 1WB, United Kingdom.
E-mail address: b.jana@shu.ac.uk (B.D. Jana).

https://doi.org/10.1016/j.wear.2022.204605
Received 6 October 2022; Received in revised form 7 December 2022; Accepted 21 December 2022
Available online 24 December 2022

fracture, and cracking) may show a variation as compared to the microstructure of components manufactured via the melting and casting route.

1.2. Solid particle erosion

It is now well known that solid particle erosion resistance is not an intrinsic material property; it depends on the operating conditions used. Process parameters, such as erodent shape and size, impact velocity, slurry concentration and impingement angle, are known to influence erosion rate significantly [16,17].

Material removal mechanism in solid particle erosion has been extensively studied for ductile and brittle materials in various operating conditions, including at different impingement angles [11,18]. At normal impact angles, solid particle erosion of ductile material is caused by local plastic deformation of the substrate and eventual removal of the deformed material by repeated erodent impacts [19–21]. One of the well-perceived theories for the material removal mechanism at normal impact angles is based on the removal of extruded "lips" of the deformed substrate in the form of platelets [20–22]. Each indenting erodent will cause a localised plastically deformed zone which, depending on the contact conditions, can lead to the formation of a crater with extruded lips all along its rim. These lips are removed by the subsequent erodent impacts sufficient to meet the failure strain requirement [21]. In contrast, at oblique impact angles, the mechanism has been well accepted to be based on ploughing and cutting, and the cutting mechanism can be of Type-1 and Type-2 [17].

1.3. Present work

Due to virtually no published data, this study aimed to systematically investigate the slurry erosion behaviour of pure Ta manufactured via PM route. As the slurry consisted of deionised water and SiC particles, corrosion effects have not been considered in this study.

The objectives of the study were to investigate the rate of erosion as a function of different process parameters, i.e., slurry concentration, particle geometry, velocity, and impact angle. The objectives also included a detailed wear scar analysis to understand the material removal mechanism for normal and oblique impact erosion. This information would be crucial for accurate modelling of the complex erosion process. In addition, this study will feed forward into the successive investigation to be conducted on the aqueous erosion-corrosion behaviour of the Ta (under more aggressive medium with different pH values).

2. Experimentation

2.1. Materials and characterisation

The tantalum (Ta) specimens of 30 mm diameter and 5 mm thick used in this study were obtained from Rutherford Appleton Laboratory (RAL), UK. These samples were 99.9% pure Ta manufactured via PM route. The samples were cut from an unused ISIS spallation target made of hot isostatically pressed pure Ta cladded to a tungsten (W) core; the design and manufacturing of the tantalum-clad tungsten spallation target have been presented elsewhere [4].

The Ta microstructural grain size, see Table 2, was measured by the linear intercept method using Image J software according to ASTM E112-12 [23].

X-Ray Diffraction (XRD) studies (Fig. 4) were performed using an Empyrean X-ray diffractometer (Malvern Panalytical, the Netherlands) using a Co-Kα X-ray source ($\lambda = 1.79$ Å). The voltage and current were 40 kV and 30 mA, respectively. The samples were scanned using a Bragg-Brentano geometry ($2\theta = 20°$-$120°$) with a step size of 0.013 ($°2\theta$) and step time of 34.17s. The crystallite sizes within the grains, see Table 2, were calculated by the Scherrer equation by measuring the peak broadening at half the maximum intensity (FWHM) using the X'Pert Highscore Plus software.

The hardness of the Ta test sample, see Table 2, was measured using a Vickers micro-hardness tester (Duramin Struers-40 AC3, Struers LLC, United States). A matrix of 25 indents (area of 25 mm × 25 mm) was utilised to measure the hardness value. The Young's modulus of the Ta sample was measured in a nano indentation tester (CSM Instruments SA) using Berkovich indenter, and the value is shown in Table 2.

The density of the Ta specimen was measured using the displacement method in distilled water, and the value obtained was 16.65 gcm^{-3}. This value is 99.9% of the theoretical density of Ta, 16.67 gcm^{-3} [24].

The test specimens were metallographically polished involving grinding using SiC emery papers up to 2500 grit, followed by fine polishing using colloidal silica suspension fluid to obtain a mirror like finish. These polished samples were then etched using etchant (30% HNO_3 of 48% strength + 70% HF of 48% strength) through the immersion process (45 s To 2 min) to reveal the microstructure. An optical microscope (Olympus BX51 M, Japan) was used to image surfaces appropriately, whereas Scanning Electron Microscope (SEM) imaging was performed using Quanta 650 and NOVA-NANOSEM (FEI, The Netherlands) electron microscopes. Erosion experiments were performed on the mirror-like finish polished surfaces. An electronic microbalance (Ohaus PA114C, Fisher Scientific, UK) having the least count of 0.0001 mg was used to measure the mass loss of eroded samples in each experiment.

For comparison, aqueous slurry erosion studies were also performed on Aluminium (Al) (99.9% pure) specimens of 30 mm diameter by 5 mm thick. Pure Al was chosen as it is one of the most researched metals from the erosion point of view, with a greater consensus on its performance and erosion mechanisms. The Al samples were manufactured via the melting and casting route with a measured density of 2.7 gm. cc^{-1} and a hardness of 100 HV_5.

2.2. Slurry erosion testing

The slurry erosion testing was conducted on an impinging jet aqueous erosion-corrosion apparatus developed at the National HIPIMS Technology Centre based at Sheffield Hallam University, UK. The apparatus is based on the principle of an impinging jet system reported by Zu et al. [25] and Purandare et al. [26]. The schematic of the impinging jet erosion-corrosion test apparatus is shown in Fig. 1. The rig consists of a slurry chamber (inner tank consisting of abrasive erodent particles with test solution) and an outer tank referred to as the solution chamber. Due to the Venturi effect, slurry from the slurry chamber is syphoned into the ejector, which then mixes with the test solution entering the ejector through the inlet nozzle. This mixture is then forced out through the ejector and bombarded the specimen placed directly in front of the exit nozzle. After striking the specimen, the erodent particles return to the 'fluidised' slurry chamber whereas the excess solution is returned to the solution chamber and then to the pumps after passing through a series of mesh filters. Thus, a consistent velocity (±5% of the set value) and concentration of particles in the slurry (±2 wt% of the desired value) can be maintained throughout the stipulated test time. A dedicated specimen holder, which can be rotated around its horizontal axis facilitates exposure of a selected area of the specimen surface to the impinging jet at different angles ranging from 20° to 90°.

2.3. Experimental matrix and its description

In order to thoroughly investigate the erosion behaviour of the Ta specimens, a large experimental matrix consisting of different impact angles, slurry concentration and impact velocity was chosen. Table 1 provides these experimental parameters in detail. The diameter of the exit nozzle was 6.5 mm and the distance between the specimen surface and the exit nozzle was maintained at 15 mm, whereas the solution was at ambient temperatures (22–24 °C) for all the experiments.

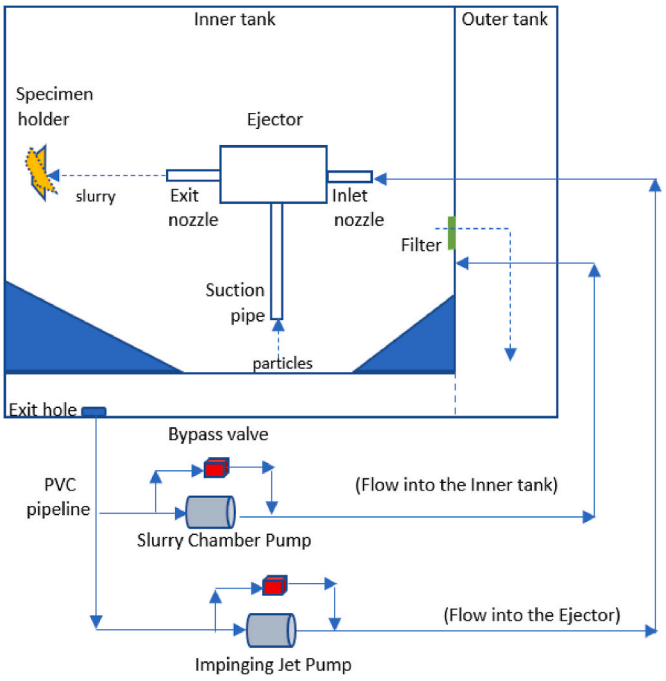

Fig. 1. Impinging jet aqueous erosion apparatus schematic.

Three sets of experiments were conducted for slurry erosion of the Ta specimens. In Set-1, using the SiC slurry concentration of 10 wt% and impact velocity of 5 ms^{-1}, the erosion rates of Ta were measured at different particle impact angles of 20°, 30°, 45°, 60°, and 90°; it revealed a peak erosion rate at 30° impact angles. In Set-2, using impact velocity of 5 ms^{-1}, the erosion rates of Ta were measured using different SiC slurry concentrations (wt. % - 3, 5, 7, and 10%) at both 30°and 90° impact angles; it revealed a peak erosion rate at 7 wt% slurry concentration. In Set-3, using the SiC slurry concentration of 7 wt%, the erosion rates of Ta were measured at different velocities (5, 4, and 3 ms^{-1}) at both 30°and 90° impact angles. For comparison, the erosion rates of Al samples were measured at 30° and 90° impact angles using the SiC slurry concentration of 7 wt% and impact velocity of 5 ms^{-1}.

For each experiment, specimens were carefully washed with Industrial Methylated Spirit (IMS), followed by deionised water and then hot air dried (using a handheld drier) before being measured on the electronic balance. Each erosion experiment lasted for 1 h and experiment at the particular condition was repeated three times for measuring the repeatability. An average of 4 mass loss readings was considered from a total of 6 measurements - first and last readings were ignored to achieve data consistency. The erosion rate (gg^{-1}), the ratio of target material mass removal rate (gs^{-1}) to the slurry particle mass flow rate (gs^{-1}), was calculated from the corresponding mass loss values, and an average erosion rate from three experimental repetitions was considered for this study.

The erodent used in this test was angular SiC particles (supplied by Hodge Clemco, UK) with 98.5% purity and particle sizes ranging from 500 to 710 μm. The density and hardness of the particles are 3100 kg m^{-3} and 25,500 MPa respectively. An SEM image of these erodent particles is shown in Fig. 2.

2.4. Selection of test conditions

A high number of pilot experiments were conducted to identify a suitable test condition that provides a measurable wear rate of Ta within the 1-h test duration. Based on the pilot results, the erodent size (500–710 μm), impact velocity (3,4 and 5 ms^{-1}) and concentrations (3, 5,7 and 10 wt%) were chosen for this study.

Being radioactive in nature, the contaminants in the deionised cooling water loop of the ISIS target were not analysed; it is speculated that the contaminants are very fine in size and in the order of few tens to hundreds of micrometres. This study aims to understand the slurry erosion response of Ta with special emphasis on identifying the erosion mechanism, which is previously unreported. The understanding gained in this preliminary study will be used by RAL for formulating further studies to achieve their overall aim to improve the service life of their ISIS spallation neutron source target.

2.5. Predicting mechanism of erosion

In the process of slurry erosion, the material removal mechanism depends upon the properties of erodent particles and target material

Table 2
Summary of the tantalum characterisation results.

Material	Grain Size (μm)	Crystallite Size (Å)	Hardness (HV_2)	Young's Modulus (MPa)
Pure Tantalum (100%)	65 ± 15	402 ± 112	89 ± 3	195 ± 6

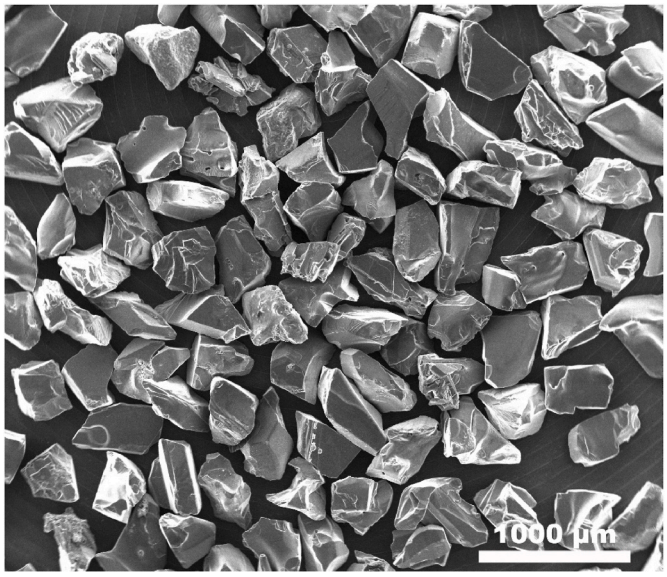

Fig. 2. SEM micrograph of SiC sand (500–710 μm) with different shapes of the particles (secondary imaging x47).

Table 1
Test matrix* detailing different set of experiments.

Experimental Set	Impact Angle (deg.)					Impact Velocity (ms^{-1})			SiC Concentration (wt.%)			
	20	30	45	60	90	3	4	5	3	5	7	10
1	✓	✓	✓	✓	✓			✓				✓
2		✓			✓			✓	✓	✓	✓	✓
3		✓			✓	✓	✓	✓			✓	

*SiC particle size of 500–710 μm, Velocity ± 5%, Concentration ± 2 wt%.

[27–29]. Therefore, in the present study, an effort was made to unravel the erosion mechanisms at oblique impact at 30° and at normal impact at 90° angles by analysing the SEM images of the erosion scar in detail.

3. Results

3.1. Material characterisation

Table 2 summarises the mechanical properties, grain size, and crystalline size, for the Ta specimens used in this work. Fig. 3 shows a typical optical microstructure of the etched Ta specimen; it reveals a non-uniform grain distribution with an average grain size of around 65 μm. It also shows the grain structure consisting of both low and high-angle grain boundaries. As the Ta specimens were manufactured via the PM route, the presence of these low and high angle grain boundaries is expected, and these were found to influence the overall erosion mechanism identified for the Ta specimens (as discussed in section 4).

In addition, as seen in the image (Fig. 3), the microstructure was free of any signs of porosity; this is consistent with the Ta specimens having a density of 16.65 gcm^{-3}, which is 99.9% of its theoretical density (16.67 gcm^{-3} [24]).

The XRD diffractogram of the Ta specimen is shown in Fig. 4. Through comparison of the powder diffraction file (PDF Card 4–788), it confirms that the Ta specimen is body centred cubic (BCC) crystal structure of 100% tantalum. The diffractogram shows a dominating and near similar contributions of (110), (200) orientation and a strong contribution of (211) orientation. Peak angles very closely resembled to those of an unstressed compacted powder (PDF card Ref 00-004-0788).

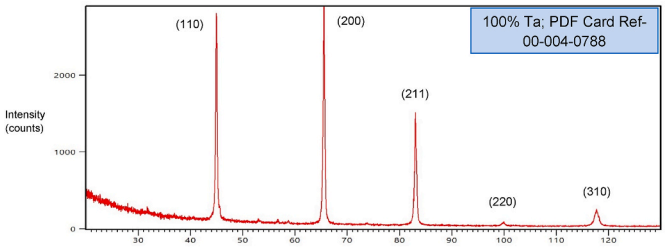

Fig. 4. X-ray diffraction (XRD) pattern of tantalum.

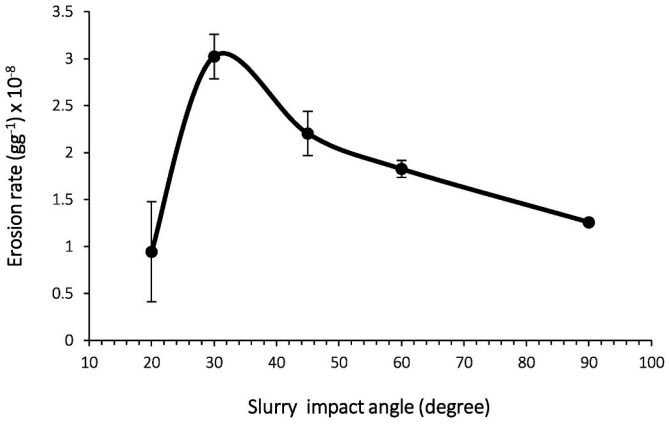

Fig. 5. Erosion rate versus impact angle for tantalum (velocity 5 ms^{-1}; SiC slurry concentration 10 wt%).

3.2. Distilled water slurry erosion

3.2.1. Effect of impact angle

Fig. 5 shows erosion rate versus impact angle plot for Ta specimens. As stated earlier, in this study erosion rate (gg^{-1}) were calculated as the ratio of target material mass removal rate (gs^{-1}) to the slurry particle mass flow rate (gs^{-1}). As observed in Fig. 5, among all the impact angles tested of 20°, 30°,45°, 60°, and 90° respectively, the erosion rate was maximum at 30° and then reduced to less than one-half of the maximum erosion rate at normal impact angles. This is consistent with the published data for the erosion of most ductile metals under dry particulate erosion conditions [17,31], which typically show a maximum erosion rate at an impact angle between 20° and 30°, and that falls to one-half to one-third of the peak erosion rate at normal impact angles.

3.2.2. Effect of particle concentration

Fig. 6 shows erosion rate for Ta specimens as a function of slurry concentration at both 30° and 90° impact angles. A very similar trend was found for both the impact angles. Among all the concentrations tested (i.e. 3, 5, 7, and 10% SiC in deionised water), the erosion rate initially increased up to an intermediate concentration of 7 wt% followed by a decrease as the concentration reached 10 wt%. Albeit erosion rate is expected to increase with slurry concentration [27,32], the reduced erosion observed at the higher slurry concentrations of 10 wt% was likely due to the combination of the test geometry effects [29, 33–35] and/or the shielding effect [34]. Albeit not verified in this study, it is expected that despite the increase in solution particles concentration and the fixed sample distance of 15 mm from the exit nozzle (with a 6.5 mm diameter), not all the particles will be able to establish contact with the sample surface. At a given moment, particles impacting the surface will shield the same surface from the impacts of the subsequent particles. This shielding effect, along with some interaction among the particles (that increases with particle concentration) may be responsible for the drop in erosion [33]. At lower impact angles of 20° or less, the test geometry results in a pronounced sliding action of the particles rather than a full-fledged surface particle interaction and could explain the drop in

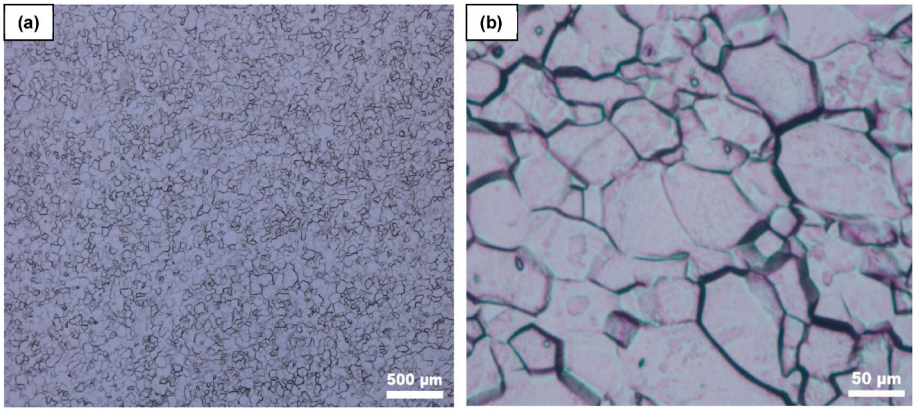

Fig. 3. Optical micrographs of the etched tantalum specimen at different magnifications: (a) x50 (b) x500 showing high angle grain boundaries.

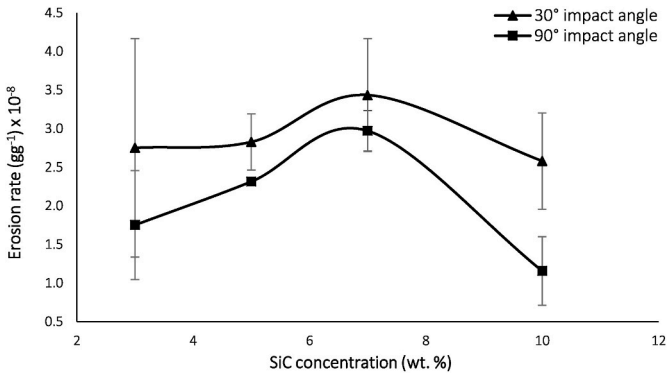

Fig. 6. Erosion rate versus SiC slurry concentration for tantalum (impact velocity 5 ms^{-1}).

the erosion rate as well as a larger error margins in these conditions.

3.2.3. Effect of impact velocity

The effect of impact velocity on the erosion for Ta specimens was investigated by subjecting the specimens to a jet velocity of 3 ms^{-1}, 4 ms^{-1}, and 5 ms^{-1}. The slurry concentration in these cases was maintained at 7 wt% as it emerged as the most damaging (for the conditions chosen in this study). Fig. 7 shows erosion rate as a function of impact velocity at 30° and 90° impact angles. As estimated, irrespective of the impact angle, the erosion rate increased linearly with impact velocity - an exception was observed at 3 ms^{-1} for 30° impact.

Unlike dry erosion tests, which generally happen at a high strain rate, temperature-induced deformation of the substrate was not expected in slurry erosion, especially in the velocity range up to 5 ms^{-1} considered in this study [36,37]. Therefore, the slurry erosion mechanism was purely dominated by the local mechanical deformation at the impact site, and the severity of the deformation increased with particle impact velocity. Under such conditions, erosion loss is expected to have a linear relationship with impact velocity; hence, the trend observed in Fig. 7.

The results at 3 ms^{-1}, for both 30° and 90° impact angles show a variation from the general trend, as shown in Fig. 7. In these situations, the specimens may have a few broken particles embedded in the matrix or trapped underneath the plastically deformed materials and voids, resulting in an artificial mass gain. This could well explain the large error margins for these test results. The mass gain was significantly higher at the lower impact velocity of 3 ms^{-1} for oblique impact of 30° and could be related to the unique erosion mechanism observed for the Ta specimens. The results also show that the severity of the erosion loss is higher at 30° than that at 90° impact.

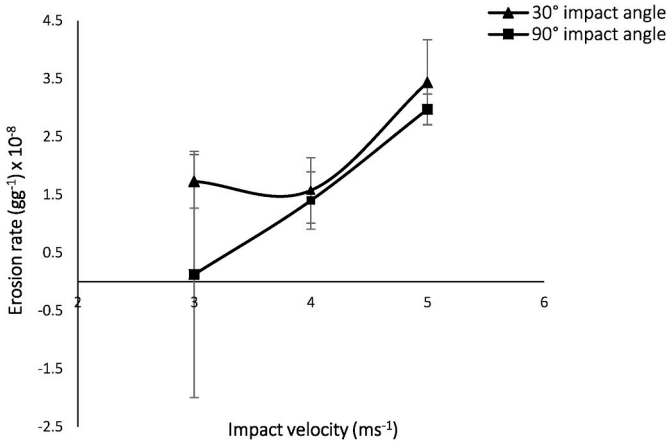

Fig. 7. Erosion rate versus impact velocity for tantalum (SiC slurry concentration 7 wt%).

3.2.4. Comparison with the reference Al sample

Fig. 8 shows erosion rate of the Ta specimen compared to the Al specimen at 30° and 90° impact angles. Both the materials were tested under the same conditions, which included the impact velocity of 5 ms^{-1} and the SiC slurry concentration of 7 wt%.

The erosion rate of the Ta was significantly higher than the Al at both the impact angles tested, see Fig. 8. At 90° impact angles, the difference was by a factor of 5, whereas at 30° was by a factor of 1.5.

As Ta has a significantly higher density than Al (2.7 gcm^{-3}), a comparison of the volumetric erosion rates (cm^{3}g^{-1}) may also be of interest to many researchers working in the field; those values are as follows: at 90°, the volumetric erosion rate of Ta and Al were 0.1785 and 0.2143 (cm^{3}g^{-1}) respectively, whereas at 30° that of Ta and Al were 0.2064 and 0.7961 (cm^{3}g^{-1}). Note that the volumetric erosion rates (cm^{3}g^{-1}) of the specimens were calculated as the ratio of the measured gravimetric erosion rate (gg^{-1}) to its density (gcm^{-3}). As expected, the volumetric erosion rates of the Ta and Al specimens show a reverse trend than that observed for the gravimetric erosion rates of the specimens.

3.3. Wear scar analysis – effect of impact angles

Fig. 9 shows the SEM micrographs of the eroded surface (wear scars) for the Ta specimens formed at 90° impact angles, 5 ms^{-1} impact velocity, and 7 wt% SiC concentration. For comparison, the SEM images for the reference Al specimens (tested under the same conditions) are also shown (Fig. 9c and d). The wear scars on Ta specimens (Fig. 9a and b) contained the following typical features: (1) a hill-and-valley topology all over the surface, (2) grain boundary cracks (arrow A), (3) lip breakage contributing to the overall erosion loss of the material (arrow B), (4) fragmented erodent (SiC) particles embedded in the wear scar (arrow C), (5) abundance of voids/cavities (appearance of black spots or blemishes) all over the surface covering both the hills and valleys (bright contrast areas in the images resulting due to sharp edges). These features are discussed in detail in subsequent sections.

In contrast, the wear scars on Al specimens (Fig. 9c and d) consisted of a hills-and-valley topology, extruded lip breakage, and evidence of fragmented erodent particles embedded in the wear scars. This is consistent with the published erosion mechanism for most ductile materials at normal impact angles [38,39]. In addition, unlike the Ta, the voids/cavities were not present in the wear scars formed on the Al.

Fig. 10 shows the SEM micrographs of the wear scars formed on the Ta specimens at 30° impact angles, 5 ms^{-1}, and 7 wt% SiC concentration (Fig. 10a and b); for comparison, the SEM images for the Al specimen tested under the same conditions are also shown (Fig. 10c and d).

Wear scars at 30° impact angles were, as expected, dominated by the

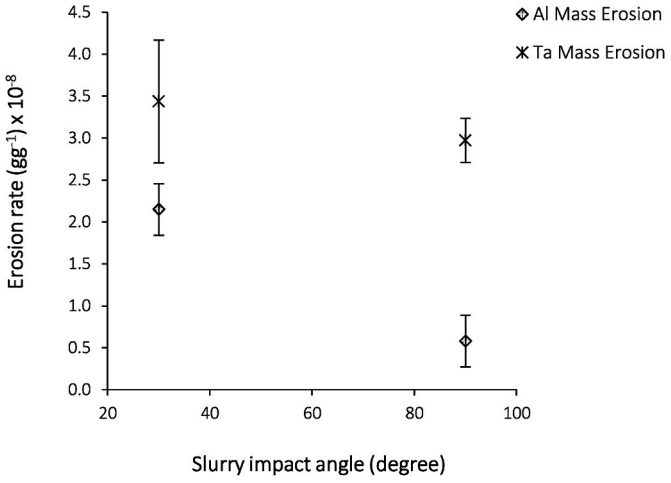

Fig. 8. Comparison of the erosion rate of the tantalum and the reference aluminium sample (Impact velocity 5 ms^{-1}; slurry concentration 7 wt%).

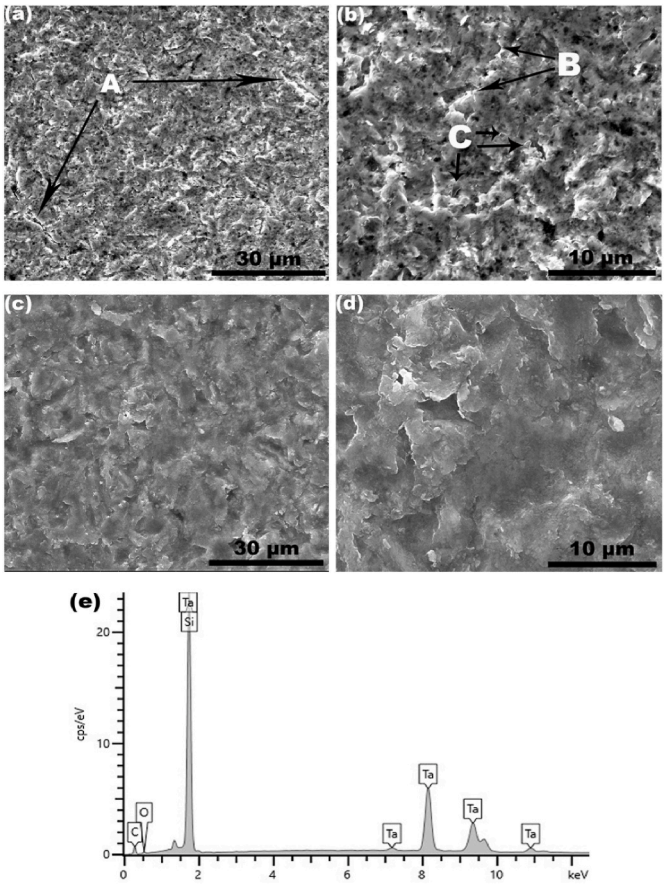

Fig. 9. Typical SEM images of the wear scars of the specimens tested at 90° impact angles (impact velocity 5 ms^{-1}; slurry concentration 7 wt%): (a) Ta (x2500), (b) Ta (x7000), (c) Al (x2500), (d) Al (x7000), (e) EDX spectrum of one of the embedded particles as shown by arrow marker C in Fig. 9(b).

cutting and ploughing mechanisms [17]. However, grain boundary cracks and an abundance of voids/cavities were also evident for 30° impact (Fig. 10a and b). The cutting mechanism was found to be as the Type-1 and Type-2. In Type-1, erodent particles roll forward, indenting the surface and pushing material into a raised lip. In contrast, in Type-2, erodent particles roll backwards and cut chips away from the surface [17]. Fig. 10 shows the Type-1 (evidence of raised lips) and the Type-2 cutting along the erodent impingement path (arrowed).

In contrast, the Al specimen (Fig. 10c and d) showed evidence of cutting (or micromachining) and ploughing at 30° impact angles; however, no evidence of voids/cavities were found.

3.4. Wear scar analysis – effect of slurry concentration

Fig. 11 shows the SEM images of the wear scars formed on Ta specimens at 5 wt% SiC concentration for 90°, see Fig. 11a and b, and 30° impact, see Fig. 11c and d; the test conditions included the impact velocity of 5 ms^{-1}.

To assess the effect of slurry concentration, the wear scars obtained at 5 wt%, as shown in Fig. 11c and d, should be compared with those at 7 wt%, as displayed in Fig. 10a and b. At 90° impact angles, increasing the SiC concentration from 5 wt%, see Fig. 11a and b, to 7 wt%, see Fig. 9a and b, showed the same hill-and-valley topology with an abundance of voids/cavities. However, at higher concentrations (7 wt%), the wear scars appeared comparatively smother due to excessive lip breakages, see Fig. 9b. The excessive lip breakage was also responsible for the high erosion loss observed at 7 wt% compared to 5 wt% (Fig. 6). In addition, the grain boundary cracks appeared to be more pronounced at 7 wt% compared to 5 wt% for 90° impact.

The effect of slurry concentration at 30° impact angles was similarly found to be more pronounced (in terms of the severity of lip breakage) as the SiC concentration was increased from 5 wt% (Fig. 11c and d) to 7 wt % (Fig. 10a and b). As expected, the wear scars formed under both concentrations showed similar cutting and ploughing dominated mechanisms with an abundance of voids/cavities. However, along the cutting/ploughing path, more extruded lips were evident at a lower concentration of 5 wt%, see Fig. 11c and d, than at 7 wt%, see Fig. 10a and b; this implies the severity of lip breakage increased with SiC concentration. As a result, the higher mass loss was obtained at 7 wt% compared to 5 wt% for 30° impact angles.

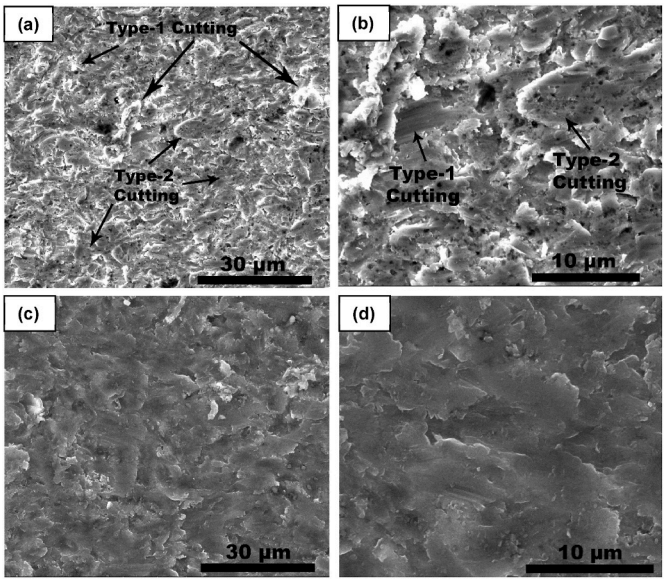

Fig. 10. Typical SEM images of the wear scars of the specimens tested at 30° impact angles (impact velocity 5 ms^{-1}; slurry concentration 7 wt%): (a) Ta (x2500), (b) Ta (x7000), (c) Al (x2500), (d) Al (x8000).

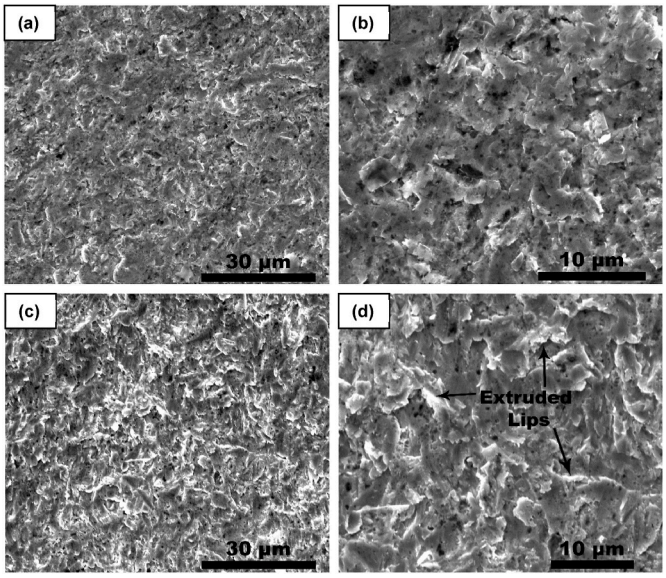

Fig. 11. Typical SEM images of the wear scars formed on Ta specimens at 5 wt % SiC concentration (impact velocity 5 ms^{-1}) for (a) 90° impact (x2500), (b) 90° impact (x7000), (c) 30° impact (x2500), (d) 30° impact (x5500).

4. Discussion

4.1. Role of erosion parameters

The Ta specimens used in this study had a hardness of 89 HV_2, and a density close to its theoretical density (16.67 gcm^{-3}). Consequently, the Ta exhibited a typical ductile material erosion response under the various slurry erosion conditions tested [27,31,34,36], with a few exceptions.

The Ta specimens, as expected, showed a higher erosion mass at oblique impact angles (peak at 30°), and the mass loss increased with impact velocity [17]. However, the effect of concentration was found to initially increase up to an intermediate concentration (peak at 7 wt%) and then decrease beyond 7 wt%. This is due to the test geometry effect and/or the shielding effect, as described earlier in the results section (section 3 of this report).

The Ta specimens exhibited more erosion mass loss than the reference Al specimen, which was by a factor of 5 at 90° impact angles and 1.5 at 30° impact angles. This may be because the Al hardness was significantly higher than the Ta (by a factor of 1.1); hence the Al is expected to show higher erosion resistance. However, the underlying erosion mechanisms (as described in subsequent sections) was also responsible for the high erosion loss recorded for the Ta specimens.

4.2. Erosion mechanisms

SEM micrographs of the wear scars on Ta specimens (Figs. 9–11) revealed the following features: (1) voids/cavities all over the surface, (2) a hill-and-valley topology at 90° impact angles, (3) cutting and ploughing mechanisms at 30° impact angles, (4) fragmented erodent embedment (albeit in limited quantities) into the subsurface. These features are discussed below using the underlying theories of ductile material erosion.

4.2.1. The formation of voids/cavities

As erodent impacts cause localised indentation deformation of the substrate, the Ta specimens was assessed under various static Vickers hardness loads. Fig. 12 shows the optical micrographs (generated using the inbuilt image acquisition capability of Duramin Struers-40 AC3) of the Vickers indents on the Ta specimens at 1, 3, and 5 kgf loads.

Under slurry erosion, especially at the lower velocities (up to 5 ms^{-1}), the particle rebound effect is expected to be high [40]. Therefore, the slurry erosion process is expected to involve a low strain rate leading to a condition close to quasi-static indentation similar to that observed under the Vickers hardness tests (Fig. 12).

Fig. 12 shows clear evidence of grain boundary sliding, which increased as the indentation load was increased from 1 kgf to 5 kgf. The grain boundary sliding was due to the movement of high angle grain boundaries present in the Ta microstructure (Fig. 3). The formation of voids/cavities due to grain boundary sliding has been extensively studied before; it has been suggested to be operative only under a low strain rate condition [41]. In this study, as the test conditions involved a low strain rate associated with the slurry impact velocity only up to 5 ms^{-1}, the grain boundary sliding is recommended to be the dominant mechanism for forming most voids/cavities at both normal and oblique impact angles.

Evidence of void growth and coalescence due to repeated slurry impacts was also apparent, especially at the location where dislodgement of a complete grain was evident at higher magnification SEM micrographs (arrowed in Fig. 13). The dislodged grain areas also looked like cavities at a lower magnification (Fig. 11a and b). The growth and coalescence of the voids were also responsible for the large grain boundary cracks observed in the SEM images (Fig. 9a). The grain dislodgement significantly contributed to the overall erosion loss of the Ta specimens investigated here (further discussed in subsequent sections).

Further scrutiny of the high magnification SEM images (Fig. 13) revealed these voids/cavities were almost all over the eroded surface, including the hills (or extruded lips) and the valleys (or impact craters) at both normal and oblique impact angles. This suggests that some of these voids remained at a microscopic size under the test conditions and could not grow enough to cause void-coalesce and eventual grain dislodgement. The direct effect of 'lip weakening' due to these voids and its removal due to subsequent impacts is difficult to quantify.

It is also known that voids/cavities in deformed metals can also form due to low angle grain boundary movement, especially at the triple point [42]. However, this mechanism is generally operative at high strain rates, significantly higher than that available for slurry erosion; hence is not expected under the slurry erosion conditions used in this study.

4.2.2. Material removal mechanisms

The primary material removal mechanisms from the Ta surface were plastic deformation at normal impact angles, whereas cutting and ploughing at oblique impact angles. In addition, grain dislodgement due to void coalescence (as stated earlier) was also a major material removal mechanism at both the impact angles. However, the contribution from the individual mechanism was not quantifiable in this study.

As observed from the SEM images of Figs. 9–13, the plastic deformation at normal impact angles was responsible for the hill-and-valley surface topology for the Ta specimens, see Fig. 9a and b; this was similar to the classical ductile material erosion mechanism observed for the reference Al specimen, see Fig. 9c and d. However, the voids/cavities were an additional feature found only for the Ta specimens. Material removal under normal impact can happen through a number of well-accepted theories [19–21]. However, the major mechanism of material removal from the Ta specimens was found to be through lip breakage from the "hills" region. This was particularly evident when the SiC concentration increased from 5 wt%, see Fig. 11a and b, to 7 wt%, see Fig. 9a and b. However, material removal from the "valleys" is also possible, but evidence of this was not very clear in this study. In addition, material loss through complete gain dislodgement was also evident at normal impact angles, see Fig. 13a; this was due to void nucleation and coalescence, especially at the high angle grain boundary.

At oblique impact angles, the mechanism was cutting and ploughing,

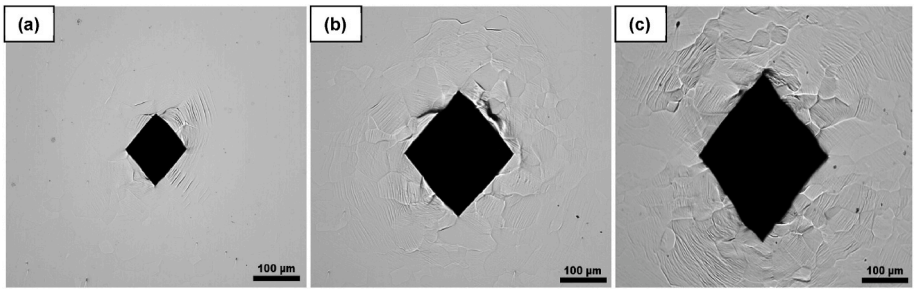

Fig. 12. Optical micrographs of Vickers indentations on the unattached polished Ta under various loads: (a) 1 kgf, (b) 3 kgf, and (c) 5 kgf.

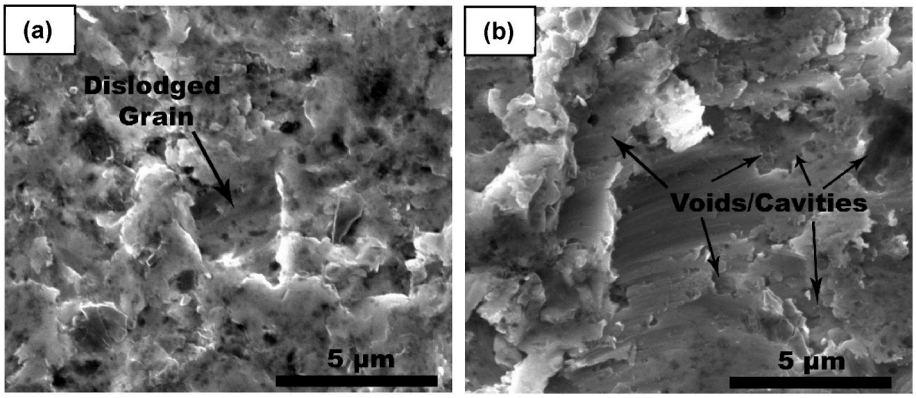

Fig. 13. Typical SEM images of the wear scars on Ta specimens tested under erosion conditions of 7 wt% slurry concentration, 5 ms^{-1} velocity for (a) 90° impact (x15000), (b) 30° impact (x15000).

as evident in the SEM images for the Ta specimen, see Fig. 10a and b. This is similar to the typical ductile material erosion, as observed for the reference Al specimen, see Fig. 10c and d [43]. However, the voids/-cavities were once again found to be an additional, prominent feature for the Ta at oblique impact angles, see Fig. 13b. Types of all the mechanisms that prevailed at oblique impact angles are described in detail in the results section (section 3 of this report).

4.2.3. Erodent embedment in the substrate

The Ta specimens used in this study had a hardness of 873 MPa, whereas that of the SiC particles, was 25,500 MPa. Hence the effect of particle impact on the particle breakage is speculated to be very low. Despite this, fragmented erodent particles, albeit in small quantities and sizes of a few hundred nanometres in dimensions, were found to be embedded in the target, which resulted in mass gain by the specimen at some test conditions, see Fig. 7. Few other researchers have also reported mass gain due to erodent embedment [42,44]. In this study, fragmented SiC erodents were found to be locked in the grain boundary cavities/voids, see Fig. 9b. Considering the size of voids of around 1–2 µm, compared to that of the erodent of 500–710 µm, the embedded particles were fragmented erodent particles, which were generated due to particle interactions within the rig. The fragmented erodents can also get embedded inside the subsurface of a healthy grain (considering the hardness difference between the two) [42]. It was not possible to identify any such entrapment of sharp and minuscule particles in this study.

5. Conclusions

The study leads to the following conclusions.

1. The Ta specimens displayed a typical ductile material erosion response with higher erosion mass loss at oblique impact angles (peak at 30°), which increased with increasing velocity.
2. For the current set of conditions (velocities, particle type, shape and size), the erosion mass loss for the Ta specimens increased with slurry concentrations up to an intermediate concentration (7 wt%) and then reduced. The increased particle interaction at higher concentrations is suggested to be the reason for the reduced mass loss at higher concentrations.
3. SEM micrographs revealed an abundance of voids/cavities distributed all over the eroded surface of the Ta specimens. These were suggested to be formed mainly due to the high angle grain boundary sliding. The high angle grain boundary was a characteristic microstructural feature of the Ta specimens manufactured via PM route.
4. Wear scar analysis from the Ta specimens also revealed a macroscopic hill-and-valley surface topology at 90° impact angles, whereas a cutting/ploughing topology at 30° impact angles.
5. The material removal mechanism for the Ta specimens was found to be supported by (i) lip breakage due to repeated erodent impacts at normal impact angles, (ii) micro-cutting and ploughing at oblique impact angles, and (iii) dislodgement of grains due to grain boundary void coalescence at both 90° and 30° impact angles.

Author contributions

J.S. Chouhan: Data Curation, Writing- Original Draft Preparation; B. D. Jana: Conceptualization, Research Methodology, Supervision, Writing - Review & Editing, Project administration, Funding acquisition; Y.P. Purandare: Supervision, Research Methodology, Writing - Review & Editing (of experimental part), Visualization; A. Dey: Conceptualization, Supervision, Research Methodology, Help with Metallography, Visualization; P. Eh. Hovsepian: Research Methodology, Visualization and Technical Discussion; D. Jenkins: Conceptualization, Research Methodology, Visualization and Technical Discussion; L. Jones: Conceptualization, Research Methodology, Visualization and Technical Discussion.

Declaration of competing interest

The authors declare that they have no known competing financial interests or personal relationships that could have appeared to influence the work reported in this paper.

Data availability

Data will be made available on request.

Acknowledgement

The authors would like to acknowledge Rutherford Appleton Laboratory (RAL) UK, and SHU Materials and Engineering Research Institute (MERI) UK, for providing financial support to carry out doctoral research studies of one of the authors (J.S. Chouhan). Mr. Gary Robinson and Mr. Andrew Gregory from Sheffield Hallam University are gratefully acknowledged for their assistance in the construction of the erosion-corrosion test rig.

References

[1] S.D. Cramer, B.S. Covino, Corrosion of tantalum and tantalum alloys, Corros. Mater. 13 (2018) 337–353, https://doi.org/10.31399/asm.hb.v13b.a0003825.
[2] Y. Huang, N. Maury, N.X. Zhang, T.G. Langdon, Microstructures and mechanical properties of pure tantalum processed by high-pressure torsion, IOP Conf. Ser. Mater. Sci. Eng. 63 (2014), https://doi.org/10.1088/1757-899X/63/1/012100.
[3] R.W. Buckman, New applications for tantalum and tantalum alloys, J. Mater. 52 (2000) 40–41, https://doi.org/10.1007/s11837-000-0100-6.

[4] M.F. Masayoshi Kawai, Kenji Kikuchi, Hiroaki Kurishita, Jing-Feng Li, Fabrication of a tantalum-clad tungsten target for KENS, J. Nucl. Mater. 296 (2001) 312–320, https://doi.org/10.1016/j.jnucmat.2011.11.041.

[5] D.J.S. Findlay, ISIS - pulsed neutron and muon source, Proc. IEEE Part. Accel. Conf. (2007) 695–699, https://doi.org/10.1109/PAC.2007.4441104.

[6] T. McManamy, M. Rennich, F. Gallmeier, P. Ferguson, J. Janney, 3 MW solid rotating target design, J. Nucl. Mater. 398 (2010) 35–42, https://doi.org/10.1016/j.jnucmat.2009.10.007.

[7] A.T. Nelson, J.A. O'Toole, R.A. Valicenti, S.A. Maloy, Fabrication of a tantalum-clad tungsten target for LANSCE, J. Nucl. Mater. 431 (2012) 172–184, https://doi.org/10.1016/j.jnucmat.2011.11.041.

[8] O. Caretta, T. Davenne, P. Loveridge, C.J. Densham, Engineering considerations on targets for a neutrino factory and muon collider, J. Nucl. Mater. 433 (2013) 538–542, https://doi.org/10.1016/j.jnucmat.2012.06.015.

[9] D. Wilcox, P. Loveridge, T. Davenne, L. Jones, D. Jenkins, Stress levels and failure modes of tantalum-clad tungsten targets at ISIS, J. Nucl. Mater. 506 (2018) 76–82, https://doi.org/10.1016/j.jnucmat.2017.10.075.

[10] B.J. Hockey, S.M. Wiederhorn, H. Johnson, in: R.C. Bradt, D.P.H. Hasselman, F. F. Lange (Eds.), Erosion of Brittle Materials by Solid Particle Impact BT - Flaws and Testing, Springer US, Boston, MA, 1978, pp. 379–402, https://doi.org/10.1007/978-1-4615-7017-2_22.

[11] D. Aquaro, E. Fontani, Erosion of ductile and brittle materials, Meccanica 36 (2001) 651–661, https://doi.org/10.1023/A:1016396719711.

[12] B.S. Chahar, A.K. Pun, Erosion wear of ductile materials: a review, in: ARIMPIE-2016, ELK ASIA PACIFIC JOURNAL, 2016, https://doi.org/10.16962/ELKAPJ/SI.ARIMPIE-2016.4.

[13] O. Caretta, T. Davenne, C.J. Densham, Water erosion tests on a tantalum sample: a short communication, J. Nucl. Mater. 492 (2017) 52–55, https://doi.org/10.1016/j.jnucmat.2017.05.003.

[14] Y. Kim, D. Lee, J. Hwang, H.J. Ryu, S.H. Hong, Fabrication and characterization of powder metallurgy tantalum components prepared by high compaction pressure technique, Mater. Char. 114 (2016) 225–233, https://doi.org/10.1016/j.matchar.2016.03.005.

[15] Y. Kim, E.P. Kim, J.W. Noh, S.H. Lee, Y.S. Kwon, I.S. Oh, Fabrication and mechanical properties of powder metallurgy tantalum prepared by hot isostatic pressing, Int. J. Refract. Met. Hard Mater. 48 (2015) 211–216, https://doi.org/10.1016/j.ijrmhm.2014.09.012.

[16] Y.I. Oka, T. Yoshida, Practical estimation of erosion damage caused by solid particle impact: Part 2: mechanical properties of materials directly associated with erosion damage, Wear 259 (2005) 102–109, https://doi.org/10.1016/j.wear.2005.01.040.

[17] I. Hutchings, P. Shipway, Wear by hard particles, in: Tribology, second ed., Elsevier Ltd., 2017, pp. 206–220, https://doi.org/10.1016/b978-0-08-100910-9.00006-4.

[18] W.R. Tyfour, M.T. Hayajneh, J.M. Qasaymeh, On the models of erosive wear of ductile materials, Proc. Inst. Mech. Eng. Part L J. Mater. Des. Appl. 232 (2018) 931–938, https://doi.org/10.1177/1464420716656479.

[19] J.G.A. Bitter, A study of erosion phenomena. Part I, Wear 6 (1963) 5–21, https://doi.org/10.1016/0043-1648(63)90003-6.

[20] I.M. Hutchings, A model for the erosion of metals by spherical particles at normal incidence, Wear 70 (1981) 269–281, https://doi.org/10.1016/0043-1648(81)90347-1.

[21] G. Sundararajan, P.G. Shewmon, A new model for the erosion of metals at normal incidence, Wear 84 (1983) 237–258, https://doi.org/10.1016/0043-1648(83)90266-1.

[22] A.V. Levy, The platelet mechanism of erosion of ductile metals, Wear 108 (1986) 1–21, https://doi.org/10.1016/0043-1648(86)90085-2.

[23] A. International, Standard Test Methods for Determining Average Grain Size, 2013, pp. 1–27, https://doi.org/10.1520/E0112-12.1.4. ASTM E112-12.

[24] R. Nunes, J.H. Adams, M. Ammons, S.H. Avery, ASM handbook: properties and selection:nonferrous alloys and special-purpose materials, in: ASM Handb., ASM International, 1990, p. 3166, https://doi.org/10.1007/s004310050884, 3174.

[25] J.B. Zu, I.M. Hutchings, G.T. Burstein, Design of a slurry erosion test rig, Wear 140 (1990) 331–344, https://doi.org/10.1016/0043-1648(90)90093-.

[26] Y. Purandare, M.M. Stack, P. Hovsepian, A study of the erosion-corrosion of PVD CrN/NbN superlattice coatings in aqueous slurries, Wear 259 (2005) 256–262, https://doi.org/10.1016/j.wear.2005.01.047.

[27] D. Kumar Goyal, H. Singh, H. Kumar, V. Sahni, Slurry erosion behaviour of HVOF sprayed WC-10Co-4Cr and Al2O 3+13TiO2 coatings on a turbine steel, Wear 289 (2012) 46–57, https://doi.org/10.1016/j.wear.2012.04.016.

[28] I. Finnie, D.H. McFadden, On the velocity dependence of the erosion of ductile metals by solid particles at low angles of incidence, Wear 48 (1978) 181–190, https://doi.org/10.1016/0043-1648(78)90147-3.

[29] A.V. Levy, Y. Paul, Erosion of steels in liquid slurries, Wear 98 (1984) 163–182, https://doi.org/10.1016/0043-1648(84)90225-4.

[31] G.R. Desale, B.K. Gandhi, S.C. Jain, Effect of erodent properties on erosion wear of ductile type materials, Wear 261 (2006) 914–921, https://doi.org/10.1016/j.wear.2006.01.035.

[32] M.K. Padhy, R.P. Saini, Effect of size and concentration of silt particles on erosion of Pelton turbine buckets, Energy 34 (2009) 1477–1483, https://doi.org/10.1016/j.energy.2009.06.015.

[33] S. Turenne, M. Fiset, J. Masounave, The effect of sand concentration on the erosion of materials by a slurry jet, Wear 133 (1989) 95–106, https://doi.org/10.1016/0043-1648(89)90116-6.

[34] T. Frosell, M. Fripp, E. Gutmark, Investigation of slurry concentration effects on solid particle erosion rate for an impinging jet, Wear 342–343 (2015) 33–43, https://doi.org/10.1016/j.wear.2015.08.003.

[35] A. Mansouri, M. Mahdavi, S.A. Shirazi, B.S. Mclaury, Investigating the effect of sand concentration on erosion rate in slurry flows, in: NACE Int. Corros. 2015 Conf. Expo, Pap. No.6130, NACE International Conference Paper No.6130, Tulsa, 2015, pp. 1–10.

[36] G. Sundararajan, R. Manish, Solid particle erosion behaviour of metallic materials at room and elevated temperatures, Tribol. Int. 30 (1997) 339–359, https://doi.org/10.1016/S0301-679X(96)00064-3.

[37] B.D. Jana, M.M. Stack, A note on threshold velocity criteria for modelling the solid particle erosion of WC/Co MMCs, Wear 270 (2011) 439–445, https://doi.org/10.1016/j.wear.2010.12.001.

[38] S. Biswas, A. Cenna, K. Williams, M. Jones, Subsurface behavior of ductile material by particle impacts and its influence on wear mechanism, Procedia Eng. 90 (2014) 160–165, https://doi.org/10.1016/j.proeng.2014.11.830.

[39] B.D. Nandre, G.R. Desale, Study the effect of impact angle on slurry erosion wear of four different ductile materials, Mater. Today Proc. 5 (2018) 7561–7570, https://doi.org/10.1016/j.matpr.2017.11.428.

[40] M.M. Stack, B.D. Jana, Modeling erosion-corrosion in metals: the effects of elastic rebound and impact angle on erosion-corrosion maps, in: Mech. Electro-Chemical Interact. Under Tribocorrosion, Elsevier, 2021, pp. 191–225, https://doi.org/10.1016/B978-0-12-823765-6.00009-2.

[41] S.H. Goods, L.M. Brown, Overview No. 1. The nucleation of cavities by plastic deformation, Acta Metall. 27 (1979) 1–15, https://doi.org/10.1016/0001-6160(79)90051-8.

[42] E. Jun, Mechanisms of solid particle erosive wear for 90 degrees impact on copper and iron, Wear 74 (1982) 143–156, https://doi.org/10.1016/0043-1648(81)90200-3.

[43] Ian Hutchings, Philip Shipway, Tribology: friction and wear of engineering materials, in: Tribol. Int., second ed., Elsevier Ltd., 2017, pp. 206–231, https://doi.org/10.1016/S0301-679X(98)00079-6.

[44] C. Ayyappadas, O.S. Shanu, A. Vijayan, I.A. Mohammed, V. Vishnu, M. Shamnadh, Effect of graphene, SiC and graphite addition on hardness, microstructure and electrical conductivity of microwave sintered copper MMCs fabricated by powder metallurgy route, J. Phys. Conf. Ser. 1355 (2019), https://doi.org/10.1088/1742-6596/1355/1/012035.